

Cite This: J. Phys. Chem. Lett. 2018, 9, 6773–6778

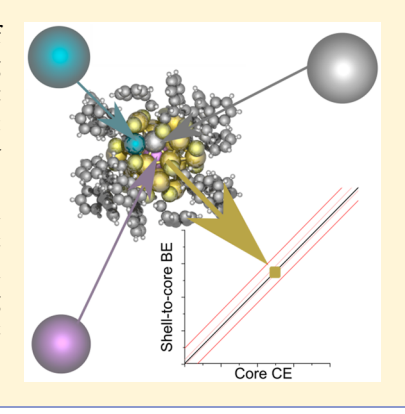
Rethinking Heterometal Doping in Ligand-Protected Metal **Nanoclusters**

Michael G. Taylor and Giannis Mpourmpakis*

Department of Chemical Engineering, University of Pittsburgh, Pittsburgh, Pennsylvania 15261, United States

Supporting Information

ABSTRACT: Heterometal doping is a promising avenue toward tailoring properties of ligand-protected metal nanoclusters for specific applications. Though successful doping has been demonstrated in several structures, the underlying reasons for the dopant preference on occupying specific locations on the nanocluster with different concentrations remain unclear. In this study we apply our thermodynamic stability model, originally developed for ligand-protected monometallic nanoclusters, to rationalize the synthetic accessibility, dopant location, and concentrations of various heterometals on ligand-protected Au nanoclusters. Importantly, we demonstrate that the thermodynamic stability theory is a significant step forward in accurately describing doping effects on nanoclusters using first-principles calculations. With our computational predictions being in excellent agreement with a series of experiments, we introduce the thermodynamic stability theory as a new method for bimetallic nanocluster prediction.



tomically precise metal nanoclusters (MNCs) have Arecently garnered extensive study because of their monodispersity and desirable physicochemical properties for numerous applications, from chemical catalysis to lightemitting devices.²⁻⁴ Toward engineering MNCs for specific applications, one approach is to dope or alloy heterometals in existing monometallic MNC frameworks. 5,6 Heterometal doping and alloying of monometallic MNCs has been shown to modulate the optical, catalytic, and stability properties of MNCs. The properties of doped MNCs are dictated by both the precise dopant locations within the MNCs¹⁰ along with dopant concentrations. 7,11 Toward control of dopants, 12-17 the first prediction (via density functional theory (DFT) calculations 18) of doped MNCs and their emergent properties highlighted the potential of doping the [Au₂₅SR₁₈] MNC. Since this initial seminal work, DFT has proven invaluable in determining the feasibility of doping within a specific MNC framework without inducing structural distortion¹³ and can give reliable dopant position-dependent energetics for several metals. 15,16 For some dopants, however, the DFT-predicted dopant locations (energetically most stable doping positions) do not match the experimental observations. Although we cannot rule out kinetic effects in the stabilization of dopants on specific locations of the MNCs, the fact that doping is a thermodynamically controlled process 14,15,21 demonstrates a potential discrepancy between theory and experiments. In addition, dopant concentration is rarely theoretically addressed (with few exceptions 10,15). This discrepancy between theory and experiments currently hinders our ability to computationally design metal-doped, ligand-protected MNCs and guide the experimental synthesis. As a result, new models are needed for understanding dopant positions and concentration effects within bimetallic MNCs. Herein, we rationalize the exper-

imentally observed dopant locations and concentration effects in atomically precise MNCs, extending the applicability of our recently developed thermodynamic stability model (TSM)²² from monometallic to alloyed MNCs.

The TSM²² states that the remarkable stability of certain MNCs with precise structure is due to a perfect balance between the chemical potentials of the metal atoms in the core region of the MNCs and the interfacial shell. The MNC core region chemical potential is roughly equivalent to the metal core cohesive energy (CE), while the interfacial shell chemical potential is equivalent to the shell-to-core binding energy (BE). When the shell-to-core BE equals the core CE, a MNC should be synthetically accessible, according to the TSM. For more details on the calculation of these energetic factors in the TSM used, see the discussion in the Supporting Information. Here, we first applied the TSM on monometallic fully ligated systems, rationalizing the stability of the experimental $\text{Au}_{18}(\text{SC}_6\text{H}_{11})_{14},^{23}$ $\text{Au}_{24}(\text{SCH}_2\text{PhC}(\text{CH}_3)_3)_{20},^{24}$ $[\text{Au}_{25}(\text{SC}_2\text{H}_4\text{Ph})_{18}]^{-,25}$ and $\text{Au}_{38}(\text{SC}_2\text{H}_4\text{Ph})_{24}$ *q*-isomer²⁶ MNCs as seen in Figure 1. These structures were selected because they have been successfully doped with at least one heterometal 16,27-29 and represent DFT-tractable fully ligated MNCs. The $[Au_{25}(SC_2H_4\tilde{P}h)_{18}]^-$ MNC, especially, has been the focus of extensive study in doping.³⁰ In Figure 2 we highlight that these full-ligand structures are all well within the previously defined²² 95% prediction interval (for Au_n(SR)_m, R = CH₃ MNCs) in a parity plot between shell-to-core BE and core CE. As there is a nonzero energetic shift in the core CE and shell-to-core BEs for methyl versus full ligands (Figure

Received: August 30, 2018 Accepted: October 26, 2018 Published: October 26, 2018 The Journal of Physical Chemistry Letters

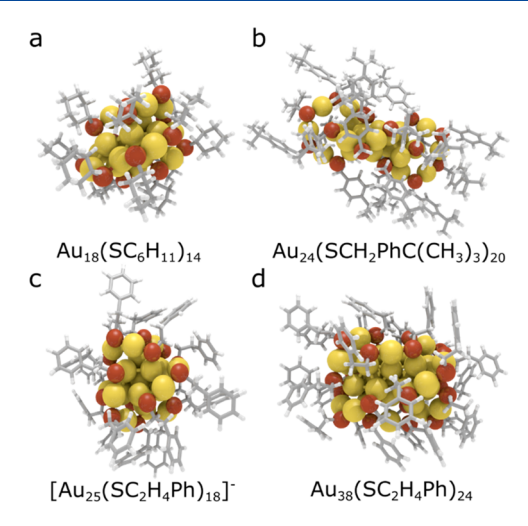


Figure 1. Density functional theory (DFT) relaxed structures of (a) are shown as sticks, whereas Au and S atoms are shown as yellow and brown balls, respectively.

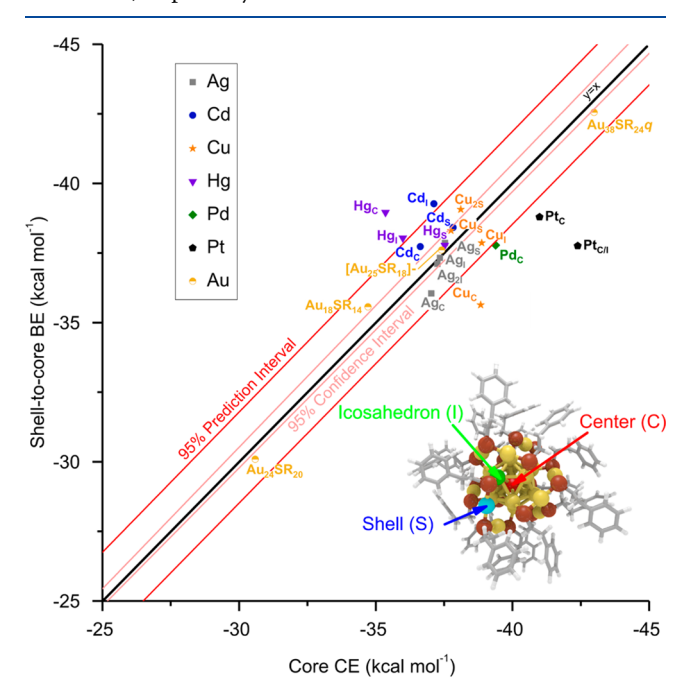


Figure 2. Thermodynamic stability parity plot between shell-to-core BE and core CE on both monometallic and doped $[Au_{25-x}M_x(SC_2H_4Ph)_{18}]^q$ MNCs (x = 1, 2) (M = Ag (q = -1), Cd(q = 0), Cu (q = -1), Hg (q = 0), Pd (q = 0), and Pt (q = 0)). Monometallic Au MNC structures are displayed in Figure 1. 95% prediction and confidence intervals displayed were generated based on previously tested²⁰ monometallic Au methyl-thiolate MNCs. The inset image shows the 3 different dopant locations (icosahedron, I; center, C; and shell, S) within the Au₂₅ MNC. All data points with metal labels correspond to doped $[Au_{25-x}M_x(SC_2H_4Ph)_{18}]^q$ MNCs with subscripts corresponding to the location(s) doped within the MNC. Energetics are shown only for MNCs that did not reconstruct during DFT geometry relaxation.

S1), herein we treat the 95% prediction interval as an approximate boundary for the synthetic accessibility of fullligand structures, serving more as a guide rather than as a strict cutoff for MNC synthesis. For example, a structure within the 95% prediction interval should be considered synthesizable,

while structures that fall within 0.7 kcal mol⁻¹ (see Figure S1 for justification of this number) of the 95% prediction interval may also be considered synthesizable. With this definition of synthetic accessibility for thiolate-protected MNCs within the TSM, we turn to doped MNCs.

We started by doping the $[Au_{25}(SC_2H_4Ph)_{18}]^-$ MNC structure (hereafter termed the Au₂₅ MNC) to form $[Au_{25-x}M_x(SC_2H_4Ph)_{18}]^q$ with M = Ag (q = -1), Cd (q = 0), Cu (q = -1), Hg (q = 0), Pd (q = 0), and Pt (q = 0), x = 1, 2. These metals have all been successfully doped into the Au₂₅ MNC with full -SC₂H₄Ph ligands but display distinct concentration, dopant location, and doped MNC charge (q) behavior as summarized in Table 1.3 Although MNC charge

Table 1. Tabulated Experimental Doping Results and Locations Tested for This Work within the Au₂₅ MNC along with Experimental Characterization Techniques of Doped **MNCs**

dopant, q	locations tested	experimentally observed?	experimental methods for dopant locations
Ag, -1	I, S, C, 2I	$I_{\text{n}}^{32,33} S_{\text{n}}^{21} 2I_{\text{n}}^{21}$ up to $\sim 20 \text{Ag}^{21}$	I/2I: XRD, ³² MALDI-MS; ³³ S: XRD ²¹ (in heavily doped MNC)
Cu, -1	I, S, C, 2S	I/(C), ^{33,34} S, ³⁵ 2I, ³³ up to 5Cu ³⁴	I/2I: MALDI-MS; ³³ C: UV-vis/ TD-DFT, ³⁴ S- EXAFS ³⁵
Cd, 0	I, S, C, 2I	I, ¹⁴ C ³⁶	I: XRD; ³⁶ C: XRD ¹⁴
Hg, 0	I, S, C, 2S	S, 19 C 14	S: XRD/MALDI-MS/TGA; ¹⁹ C: XRD/MALDI-MS ¹⁴
Pd, 0	I, S, C, C/I	C^{37-39}	C: MALDI-MS ^{37,38} XRD ³⁹
Pt, 0	I, S, C, C/I	C ^{40,41}	C: EXAFS/XPS, ⁴¹ MALDI-MS/NMR ⁴⁰

behavior is an important aspect in predicting doped MNC stability, 31 here we have run only the experimentally observed charge states of each MNC for the purpose of directly comparing our calculations and the TSM to all experiments. We note that the TSM may also readily be applied to MNCs with different charge states. 22 To test the ability of the TSM in rationalizing the synthetic accessibility of doped MNCs, we first focus on doped MNCs that have not been experimentally observed (utilizing information from Table 1 and Figure 2). In Figure 2 the core (C), shell (S), and icosahedron (I) distinct dopant locations within the Au₂₅ MNC are shown, and all metals were doped (one at a time) into each location. On the basis of the observed doping locations in Figure 2, we also tested one double-doped configuration for each metal in the Au₂₅ MNC. We note that the only doped MNCs that do not fall near the 95% prediction interval on Figure 2 are the Pt_{C/I,} Hg_C and Cu_C MNCs. Experimentally, Pt⁴¹ has been shown to be only monodoped to the C location in the Au₂₅ MNC, so deviation from parity for the double-doped Pt_{C/I} MNCs aligns with the experimental observation of dopant concentration. Additionally, Cu_C falling away from parity in the TSM appears to largely align with experimental observations where either the S^{34} or I^{33} sites are preferred for Cu incorporation into this MNC. The Cu_C MNC has been predicted only by comparison of time-dependent DFT (TD-DFT) calculations with ultraviolet-visible (UV-vis) spectra, representing relatively weak evidence compared to that of the Cu_S or Cu_T MNCs (see Table 1).35 Thus, all doped MNCs that deviate from the TSM in Figure 2 either have not been experimentally synthesized or show weak experimental evidence compared to other MNC isomers.

Apart from the TSM shown in Figure 2, previous work has indicated geometric reconstruction can serve as a metric for lack of stability for doped MNCs. 13 Here, we quantify reconstruction by comparing the relaxed structures of the cores of the doped MNC structures to that of the core of the Au_{25} MNC in a displacement (δ) metric (see the Supporting Information for methods). The structures and δ values of the cores of the doped MNCs are shown in Figure S2 and Table S1. From Figure S2 we highlight that the doped MNCs showing reconstruction under geometry relaxation included the $Cd_{2\nu}$ Hg_{2S} , Pd_{ν} Pd_{S} , $Pd_{C/\nu}$ Pt_{ν} and Pt_{S} MNCs. We note in Figure S3 that although some of these reconstructed MNCs follow the TSM, they are not likely to be experimentally isolated because of further reconstruction and possible transformation to other MNCs.²¹ Given Cd,³⁶ Hg,¹⁹ and Pd³⁸ have been successfully only monodoped into Au₂₅ MNCs in experiments, δ here appears to capture the lack of stability of the double-doped Cd_{2L}, Hg_{2S}, and Pd_{C/I} MNCs. Additionally, both Pd³⁹ and Pt⁴¹ have been shown to occupy only the C position within the MNC, indicating that δ further rationalizes why the Pt₁, Pt₅, Pd₁, and Pd₅ MNCs are not observed in experiments. We therefore show the combination of the TSM with core δ during geometry relaxation to be effective for screening the potentially nonsynthesizable doped MNCs.

Beyond synthetic accessibility, the TSM can also be applied to rationalize dopant location-dependent preference trends. For MNCs, such as the Pd- and Pt-doped Au₂₅, where only one doping event does not induce MNC reconstruction and the doping location energetically follows the TSM, then, the location preference assignment is trivial. For other dopants it is not as simple, and several dopant locations remain under debate in the literature (in the absence of definitive singlecrystal X-ray diffraction (XRD) results) as highlighted in Table 1. For Ag, we note in Figure 2 that all Ag-doped Au₂₅ MNCs tested did not reconstruct and fall well within the 95% prediction interval. For cases such as Ag, we propose that the distance from parity in the TSM for these MNCs can serve as a metric for dopant location preference. Thus, the Ag_I MNC is favored (XRD results) at lower doping³² concentrations and falls closest to the parity line in Figure 2. The Ag₂₁ MNC also falls close to the parity line in Figure 2, suggesting further doping is achievable, in line with experimental observations.³³ Additionally, heavily Ag-doped MNCs showed the S-locations being occupied following the filling of the I-locations,²¹ and our TSM shows (with single doping) the Ag_S MNC being the next closest to the parity line (vs Ag_I) in Figure 2. Finally, the C- location doping with Ag is predicted to be accessible by the TSM, where in Figure 2 the Ag_C falls within the 95% prediction interval. However, the Ag_C MNC falls much further away from the parity line than either the Ag_I or Ag_S MNCs, which helps explain the experimental inaccessibility of this Au_C MNC as two other doping locations are more thermodynamically favored.

Looking to dopant metals other than Ag, we note Cu was shown to likely be doped into the S site of the MNC by extended X-ray absorption fine structure (EXAFS) analysis, and it falls closest to the parity line in Figure 2. The next closest MNC laying within the 95% prediction interval in Figure 2 is the Cu_{2S} MNC, and experimental doping has been observed up to 5 Cu atoms within the MNC. Next, while still within the 95% prediction interval in Figure 2, the Cu_{I} has

been inferred from experiments by matrix-assisted laser desorption/ionization mass spectroscopy (MALDI-MS) fragment analysis (though less definitive than EXAFS results).³³ A potential experimental verification of these results would be using electrospray ionization mass spectroscopy (ESI-MS), as this analytical technique has proven more effective in rationalizing dopant positions than MALDI-MS. 42,43 Finally, the Cu_C MNC is shown to fall outside the 95% prediction interval in Figure 2 and, as discussed above, shows relatively weaker experimental evidence.³⁴ Following a similar analysis as for Ag and Cu, for Hg we note that the MNC most conclusively observed in single-crystal XRD was the Hgs MNC,19 which falls closest to the parity line of any Hgdoped Au₂₅ MNCs in Figure 2. We note that the doping of Hg into the Au₂₅ MNC gives conflicting results in the experimental literature where reports of both the ${\rm Hg_S}^{19}$ and ${\rm Hg_C}^{14}$ exist. The study reporting ${\rm Hg_C}$ indicates difficulty in properly assigning doping location based on the XRD patterns and relies on MALDI-MS fragmentation analysis to suggest the Hg_C position.¹⁴ However, the study reporting the Hg_S MNC appears conclusive as to the dopant location, combining XRD with MALDI-MS and thermogravimetric analysis (TGA) results. We therefore highlight the Hgs as more prominently observed in experiments and further note that the Hg_C MNC deviates significantly from the parity in Figure 2. Although the Hg_I MNC is also near the 95% prediction interval (i.e., potentially synthesizable) in Figure 2 (unlike Hg_C that deviates), the relative proximity of the Hgs to the parity compared to the Hg_I MNC seems to indicate stronger preference for the Hg_S MNC over the Hg_I MNCs, providing the first theoretical rationalization for the experimental observation of the Hg_S MNC. Thus, the Ag, Cu, and Hg doping results shown in Figure 2 (ranked by distance from the parity line) qualitatively agree with a series of experimental observations of both concentration and dopant location preference.

The doping location preferences for Cd within the MNC, however, first appear to slightly deviate from those in Table 1. For the Cd-doped Au₂₅ MNC, all the dopant locations appear to fall within or near the 95% prediction interval and therefore would all be predicted as synthetically accessible by the TSM. However, in XRD crystal structures of the isolated Cd-doped MNCs, only the I¹² and C³⁶ locations have been replaced by Cd. We also note that the Cd_C falls closer to the parity line in Figure 2 and therefore suggest that Cd_I could potentially be transformed to the Cd_C MNC under appropriate experimental conditions. Additionally, although the Cds is not observed in these experiments, it appears closest to the parity line in Figure 2 and does not undergo reconstruction during relaxation. This deviation of TSM from experiments, specific to Cd doping, is likely due to the high reactivity of the Cd dopant and its relative oxidation state in the Cd_S MNC. In metal exchange experiments, the Cd-doped MNC was observed to rapidly react with Hg²⁺ ions to form the Hg_S MNC, while the reverse reaction to form Cd_I from Hg_S was unfavorable. This indicates that the Hg_S MNC is more stable and the doped Cd is likely more reactive than the doped Hg.³⁶ When the doped Cd atom occupies either the C or I locations within the Au₂₅ MNC framework, it is likely shielded from further reactions with Au salts in solution, while the S-doped Cd atoms react with surrounding Au salts and are destroyed. Additionally, our previous work on doping within Au MNCs showed that difference in the charge of dopant and the Au atom replaced in a MNC (delta charge) can be tied to the relative dopant oxidation state and trends directly with the Gibbs free energy of formation of the doped MNC. ¹⁶ In Table S2 we highlight the delta charges of all the monodoped Au_{25} MNCs, showing that the Cd delta charge in Cd_S (charge compared to the equivalent Au atom in the Au_{25} MNC) shows the largest positive charge transfer. This seems to indicate the Cd in the Cd_S is closer to an oxidized form of dopant metal than in any of the other doped MNCs, in seeming agreement with the conclusion that the Cd_S is highly reactive and likely chemically unstable relative to either the Cd_I or Cd_C MNCs. Taking these special considerations for Cd into account, the TSM captures the experimental observations of Cd doping location within the Au_{25} MNC as well.

Apart from the special case of the Cd_S MNC, the TSM captures both doping locations and concentration behavior within the Au₂₅ MNC for a wide variety of metals and experimental observations. Importantly, we note that simple DFT energetics to a large extent do not capture these same trends and offer little to no insights into synthetic accessibility of doped MNCs. In Table S3 we show the relative DFT energies of the three isomers of the monodoped Au₂₅ MNCs with each metal. By utilizing only the total DFT energies shown in Table S3, we would predict Ag to occupy the I location, Cu to occupy the C and I locations, Cd and Hg to occupy only the I location, and Pd and Pt to occupy only the C location (due to the high energy difference, ~10-18 kcal mol⁻¹, between the ground state and other dopant positions). While Ag, Pd, and Pt doping locations are quite accurately captured by this method in comparison to experiments, the Hg, Cu, and Cd doping locations and energetics are not. Hg, for instance is predicted to be most stable at the I location by 10 kcal mol⁻¹ and is not observed at this position in experiments. We therefore highlight the power of the TSM over simple DFT energetics for predicting and screening heterometal doping within a MNC framework. Doped MNCs which show low total energetics but do not follow the TSM, can be viewed as intermediate structures of MNCs that will either grow in size, or change composition in a way to alter the core/shell energetics and fulfill the perfect energy balance of the TSM. We note that while experimental attempts to dope other metals (such as Ni³⁶ and Zn¹⁴ in the Au₂₅ MNC) have proven unsuccessful thus far, we focused here on metals that have been successfully doped into the Au₂₅ MNCs and rationalize the preference on doping positions. Additionally, ligands can play a role in determining the preference of doping,²¹ and our results with -CH₂CH₂Ph ligands may not be straightforwardly transferable to doped Au₂₅ MNCs stabilized by other ligands.

Beyond the ubiquitous Au_{25} MNC, we also tested doping within the $Au_{38-x}M_x(SR)_{24}$ (q-isomer) MNC with M=Pd (x=1,2) (q=0) and Pt (x=1 (q=-1), 2 (q=-2)) in the locations seen in Table 2 and Figure 3. Because of the larger computational cost of the $Au_{38-x}M_x(SR)_{24}$ system (herein termed the Au_{38q} MNC), we did not exhaustively test all doping locations but focused on the ones that were shown to remain rigid in previous theoretical work. Focusing first on the Pd-doped MNCs, we see that only one of the MNCs falls outside the "synthesizable regime", which is the Pd_{2C} MNC. In Table 2 we see that DFT 9,44 has previously predicted the Pd_{2C} to be the most stable structure. However, another experimental work showed evidence of Pd-S bonds in EXAFS analysis, 20 leading them to conclude the actual structure was largely

Table 2. Tabulated Experimental Doping Results and Locations Tested for This Work within the Au_{38q} MNC along with Experimental Characterization Techniques of Doped MNCs

dopant, q	locations tested	experimentally observed?	methods for dopant locations determination
Pd, 0	I, S, C, 2I, 2S, 2C, C/S	$2C_{1}^{9,44} C/S^{20}$	2C: DFT suggested; ^{9,44} C/S: EXAFS ²⁰
Pt, −1	I, S, C,	_	_
Pt, −2	2I, 2S, 2C, C/S	2C ⁴⁴	2C: XPS ⁴⁴

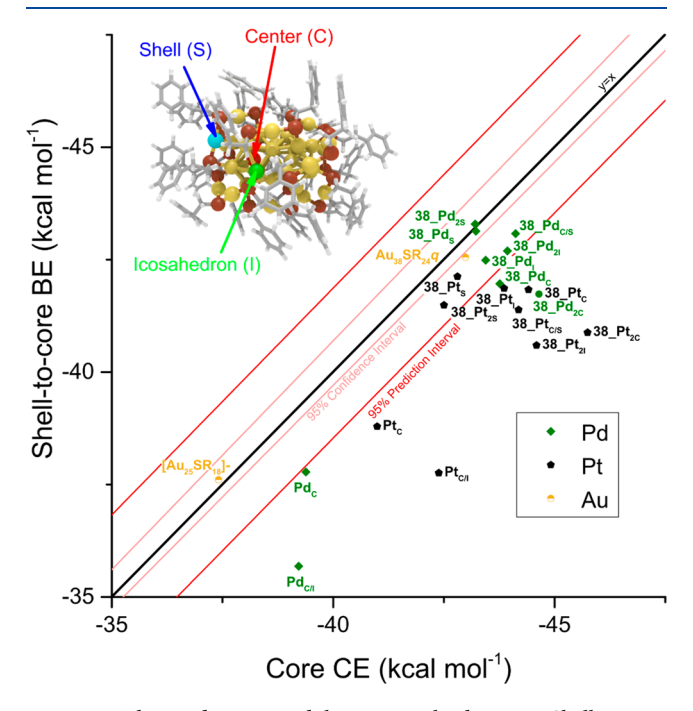


Figure 3. Thermodynamic stability parity plot between Shell-to-core BE and core CE on both monometallic and doped $[Au_{38-x}M_x(SC_2H_4Ph)_{24}]^q$ MNCs (x=1,2) (M=Pd (q=0) and Pt (q=-1,-2)). Monometallic Au MNC structures are displayed in Figure 1. 95% prediction and confidence intervals displayed were generated based on previous²⁰ monometallic Au methyl-thiolate NCs. The inset image shows the 3 different dopant locations (icosahedron, I; center, C; and shell, S) within the Au_{38q} MNC. All data points with metal labels beginning with 38 correspond to doped $[Au_{38-x}M_x(SC_2H_4Ph)_{24}]^q$ MNCs with subscripts corresponding to the location(s) doped within the MNC. None of these MNCs showed reconstruction during relaxation with DFT.

composed of either the Pd_{2S} or $Pd_{C/S}$ MNCs. Pd_{2S} and $Pd_{C/S}$ both also match the results suggested by the TSM in Figure 3, where the Pd_{2S} MNC falls closest to the parity line and the $Pd_{C/I}$ MNC is next closest of the double-doped MNCs. On the basis of the results from the TSM, we suggest, along with previous authors, 20 that the Pd is located at the S site of the Pd-doped Au_{38q} MNC, distinct from the Pd-doped Au_{2S} MNC, where the heterometal Pd is definitively doped in the C location. Finally, we turn to the Pt-doped Au_{38q} MNC. This MNC was recently reported to have a q=-2 charge and the authors utilized DFT and X-ray photoelectron spectroscopy (XPS) analysis to conclude that the only Pt dopant location within the Au_{38q} MNC would be the Pt_{2C} MNC. In the absence of a more conclusive experimental method such as XRD for Pt-location determination, we cannot rule out the stabilization of Pt at other locations of the MNC. Analysis with

TSM in Figure 3 again reveals that the S location is highly preferred in this structure, with the Pt_s and Pt_{2s} being the only two Pt-doped MNCs to fall within the 95% prediction interval. On the basis of the doping observations in the Pd-doped Au_{38q} MNC and the demonstrated ability of the TSM to capture experimental dopant locations in the Au₂₅ MNCs, we suggest that at least some of the Pt dopants are located at the S position within the Au₃₈q MNC. In analyzing the Au_{38q} MNC for doping with different metals, we have found the TSM to agree with at least one report of the Pd-doped MNC and suggest dopant locations not currently reported in literature for the Pt-doping within the Au₃₈ MNC. We have also shown that the TSM works for doping in MNCs beyond the Au₂₅ and have used the TSM to make predictions surrounding doping location within an already experimentally synthesized MNCs.

In summary, we have applied our recently published TSM for understanding doping effects and stability of ligand protected MNCs. We have shown the TSM to be a valuable extension to the current knowledge surrounding doping within MNCs, capturing a wide range of experimental observations from dopant locations to concentrations. The application of the TSM to doped MNCs represents a novel way for rationalizing doping within MNCs, moving away from simplified total-energy (DFT) calculations and significantly increasing the agreement between theory and experimental observations of doping on MNCs. We therefore view the application of the TSM to the doped MNCs as a new way to revisit doping energetics on ligand-protected MNCs. As such, it has the potential to open new avenues for accelerating bimetallic MNC discovery.

ASSOCIATED CONTENT

S Supporting Information

The Supporting Information is available free of charge on the ACS Publications website at DOI: 10.1021/acs.jpclett.8b02679.

Details of the computational methods along with figures and tables referenced in the Letter (PDF)

AUTHOR INFORMATION

Corresponding Author

*E-mail: gmpourmp@pitt.edu.

ORCID 6

Giannis Mpourmpakis: 0000-0002-3063-0607

The authors declare no competing financial interest.

ACKNOWLEDGMENTS

This work was supported by the National Science Foundation (CBET-CAREER program) under Grant No. 1652694. M.G.T. acknowledges support by the NSF Graduate Research Fellowship under Grant No. 1247842. Computational support was provided by the University of Pittsburgh Center for Research Computing and the Extreme Science and Engineering Discovery Environment supported by the NSF (ACI-1548562).

REFERENCES

(1) Zhao, S.; Austin, N.; Li, M.; Song, Y.; House, S. D.; Bernhard, S.; Yang, J. C.; Mpourmpakis, G.; Jin, R. Influence of Atomic-Level Morphology on Catalysis: The Case of Sphere and Rod-Like Gold

- Nanoclusters for CO₂ Electroreduction. ACS Catal. 2018, 8, 4996-
- (2) Chakraborty, I.; Pradeep, T. Atomically Precise Clusters of Noble Metals: Emerging Link Between Atoms and Nanoparticles. Chem. Rev. 2017, 117, 8208-8271.
- (3) Jin, R.; Zeng, C.; Zhou, M.; Chen, Y. Atomically Precise Colloidal Metal Nanoclusters and Nanoparticles: Fundamentals and Opportunities. Chem. Rev. 2016, 116, 10346-10413.
- (4) Yao, Q.; Chen, T.; Yuan, X.; Xie, J. Toward Total Synthesis of Thiolate-Protected Metal Nanoclusters. Acc. Chem. Res. 2018, 51, 1338-1348.
- (5) Jin, R.; Nobusada, K. Doping and Alloying in Atomically Precise Gold Nanoparticles. Nano Res. 2014, 7, 285-300.
- (6) Yao, Q.; Yuan, X.; Chen, T.; Leong, D. T.; Xie, J. Engineering Functional Metal Materials at the Atomic Level. Adv. Mater. 2018, 1802751, 1802751-1802751.
- (7) Negishi, Y.; Iwai, T.; Ide, M. Continuous Modulation of Electronic Structure of Stable Thiolate-Protected Au₂₅ Cluster by Ag Doping. Chem. Commun. 2010, 46, 4713-4713.
- (8) Zhao, J.; Jin, R. Heterogeneous Catalysis by Gold and Gold-Based Bimetal Nanoclusters. Nano Today 2018, 18, 86-102.
- (9) Negishi, Y.; Igarashi, K.; Munakata, K.; Ohgake, W.; Nobusada, K. Palladium Doping of Magic Gold Cluster Au₃₈(SC₂H₄Ph)₂₄: Formation of Pd₂Au₃₆(SC₂H₄Ph)₂₄ with Higher Stability than Au₃₈(SC₂H₄Ph)₂₄. Chem. Commun. **2012**, 48, 660–662.
- (10) Hartmann, M. J.; Häkkinen, H.; Millstone, J. E.; Lambrecht, D. S. Impacts of Copper Position on the Electronic Structure of $[Au_{25-x}Cu_x(SH)_{18}]^-$ Nanoclusters. J. Phys. Chem. C **2015**, 119, 8290–
- (11) Niihori, Y.; Hossain, S.; Kumar, B.; Nair, L. V.; Kurashige, W.; Negishi, Y. Perspective: Exchange Reactions in Thiolate-Protected Metal Clusters. APL Mater. 2017, 5, 053201.
- (12) Wang, S.; Abroshan, H.; Liu, C.; Luo, T.-Y.; Zhu, M.; Kim, H. J.; Rosi, N. L.; Jin, R. Shuttling Single Metal Atom Into and Out of a Metal Nanoparticle. Nat. Commun. 2017, 8, 848.
- (13) Li, Q.; Lambright, K. J.; Taylor, M. G.; Kirschbaum, K.; Luo, T.-Y.; Zhao, J.; Mpourmpakis, G.; Mokashi-Punekar, S.; Rosi, N. L.; Jin, R. Reconstructing the Surface of Gold Nanoclusters by Cadmium Doping. J. Am. Chem. Soc. 2017, 139, 17779-17782.
- (14) Wang, S.; Song, Y.; Jin, S.; Liu, X.; Zhang, J.; Pei, Y.; Meng, X.; Chen, M.; Li, P.; Zhu, M. Metal Exchange Method Using Au₂₅ Nanoclusters as Templates for Alloy Nanoclusters with Atomic Precision. J. Am. Chem. Soc. 2015, 137, 4018-4021.
- (15) Li, Q.; Luo, T.-y.; Taylor, M. G.; Wang, S.; Zhu, X.; Song, Y.; Mpourmpakis, G.; Rosi, N. L.; Jin, R. Molecular "Surgery" on a 23-Gold-Atom Nanoparticle. Sci. Adv. 2017, 3, e1603193.
- (16) Li, Q.; Taylor, M. G.; Kirschbaum, K.; Lambright, K. J.; Zhu, X.; Mpourmpakis, G.; Jin, R. Site-Selective Substitution of Gold Atoms in the Au₂₄(SR)₂₀ Nanocluster by Silver. J. Colloid Interface Sci. 2017, 505, 1202-1207.
- (17) Hossain, S.; Ono, T.; Yoshioka, M.; Hu, G.; Hosoi, M.; Chen, Z.; Nair, L. V.; Niihori, Y.; Kurashige, W.; Jiang, D.-e.; et al. Thiolate-Protected Trimetallic Au_{~20}Ag_{~4}Pd and Au_{~20}Ag_{~4}Pt Alloy Clusters with Controlled Chemical Composition and Metal Positions. J. Phys. Chem. Lett. 2018, 9, 2590-2594.
- (18) Jiang, D.-e.; Dai, S. From Superatomic Au₂₅(SR)₁₈- to Superatomic M@Au₂₄(SR)₁₈q Core-Shell Clusters. *Inorg. Chem.* 2009, 48, 2720-2722.
- (19) Liao, L.; Zhou, S.; Dai, Y.; Liu, L.; Yao, C.; Fu, C.; Yang, J.; Wu, Z. Mono-Mercury Doping of Au₂₅ and the HOMO/LUMO Energies Evaluation Employing Differential Pulse Voltammetry. J. Am. Chem. Soc. 2015, 137, 9511-9514.
- (20) Zhang, B.; Kaziz, S.; Li, H.; Wodka, D.; Malola, S.; Safonova, O.; Nachtegaal, M.; Mazet, C.; Dolamic, I.; Llorca, J.; et al. Pd₂Au₃₆(SR)₂₄ Cluster: Structure Studies. Nanoscale 2015, 7, 17012-17019.
- (21) Li, Q.; Wang, S.; Kirschbaum, K.; Lambright, K. J.; Das, A.; Jin, R. Heavily Doped $Au_{25-x}Ag_x(SC_6H_{11})_{18}^-$ Nanoclusters: Silver Goes from the Core to the Surface. Chem. Commun. 2016, 52, 5194-5197.

- (22) Taylor, M. G.; Mpourmpakis, G. Thermodynamic Stability of Ligand-Protected Metal Nanoclusters. *Nat. Commun.* **2017**, *8*, 15988.
- (23) Das, A.; Liu, C.; Byun, H. Y.; Nobusada, K.; Zhao, S.; Rosi, N.; Jin, R. Structure Determination of [Au₁₈(SR)₁₄]. *Angew. Chem., Int. Ed.* **2015**, *54*, 3140–3144.
- (24) Das, A.; Li, T.; Li, G.; Nobusada, K.; Zeng, C.; Rosi, N. L.; Jin, R. Crystal Structure and Electronic Properties of a Thiolate-Protected Au₂₄ Nanocluster. *Nanoscale* **2014**, *6*, 6458–6462.
- (25) Zhu, M.; Aikens, C. M.; Hollander, F. J.; Schatz, G. C.; Jin, R. Correlating the Crystal Structure of A Thiol-Protected Au₂₅ Cluster and Optical Properties. *J. Am. Chem. Soc.* **2008**, *130*, 5883–5885.
- (26) Qian, H.; Eckenhoff, W. T.; Zhu, Y.; Pintauer, T.; Jin, R. Total Structure Determination of Thiolate-Protected Au₃₈ Nanoparticles. *J. Am. Chem. Soc.* **2010**, *132*, 8280–8281.
- (27) Xiang, J.; Li, P.; Song, Y.; Liu, X.; Chong, H.; Jin, S.; Pei, Y.; Yuan, X.; Zhu, M. X-Ray Crystal Structure, and Optical and Electrochemical Properties of the $\mathrm{Au_{15}Ag_3}(\mathrm{SC_6H_{11}})_{14}$ Nanocluster with a Core–Shell Structure. *Nanoscale* **2015**, 7, 18278–18283.
- (28) Kumara, C.; Gagnon, K. J.; Dass, A. X-ray Crystal Structure of Au_{38-x}Ag_x(SCH₂CH₂Ph)₂₄ Alloy Nanomolecules. *J. Phys. Chem. Lett.* **2015**, *6*, 1223–1228.
- (29) Sharma, S.; Yamazoe, S.; Ono, T.; Kurashige, W.; Niihori, Y.; Nobusada, K.; Tsukuda, T.; Negishi, Y. Tuning the Electronic Structure of Thiolate-Protected 25-Atom Clusters by Co-substitution with Metals Having Different Preferential Sites. *Dalton Trans.* **2016**, 45, 18064–18068.
- (30) Kang, X.; Chong, H.; Zhu, M. Au₂₅(SR)₁₈: the Captain of the Great Nanocluster Ship. *Nanoscale* **2018**, *10*, 10758–10834.
- (31) Alkan, F.; Muñoz-Castro, A.; Aikens, C. M. Relativistic DFT Investigation of Electronic Structure Effects Arising from Doping the Au₂₅ Nanocluster with Transition Metals. *Nanoscale* **2017**, *9*, 15825–15834
- (32) Kumara, C.; Aikens, C. M.; Dass, A. X-ray Crystal Structure and Theoretical Analysis of Au_{25-x}Ag_x(SCH₂CH₂Ph)₁₈⁻ Alloy. *J. Phys. Chem. Lett.* **2014**, *5*, 461–466.
- (33) Gottlieb, E.; Qian, H.; Jin, R. Atomic-Level Alloying and Dealloying in Doped Gold Nanoparticles. *Chem. Eur. J.* **2013**, 19, 4238–4243.
- (34) Negishi, Y.; Munakata, K.; Ohgake, W.; Nobusada, K. Effect of Copper Doping on Electronic Structure, Geometric Structure, and Stability of Thiolate-Protected Au₂₅ Nanoclusters. *J. Phys. Chem. Lett.* **2012**, *3*, 2209–2214.
- (35) Yamazoe, S.; Kurashige, W.; Nobusada, K.; Negishi, Y.; Tsukuda, T. Preferential Location of Coinage Metal Dopants (M = Ag or Cu) in $[Au_{25-x}M_x(SC_2H_4Ph)_{18}]^-$ (x = 1) as Determined by Extended X-ray Absorption Fine Structure and Density Functional Theory Calculations. *J. Phys. Chem. C* **2014**, *118*, 25284–25290.
- (36) Yao, C.; Lin, Y. J.; Yuan, J.; Liao, L.; Zhu, M.; Weng, L. H.; Yang, J.; Wu, Z. Mono-Cadmium vs Mono-Mercury Doping of Au₂₅ Nanoclusters. *J. Am. Chem. Soc.* **2015**, *137*, 15350–15353.
- (37) Qian, H.; Barry, E.; Zhu, Y.; Jin, R. Doping 25-Atom and 38-Atom Gold Nanoclusters with Palladium. *Wuli Huaxue Xuebao* **2011**, 27, 513–519.
- (38) Negishi, Y.; Kurashige, W.; Niihori, Y.; Iwasa, T.; Nobusada, K. Isolation, Structure, and Stability of a Dodecanethiolate-Protected Pd₁Au₂₄ Cluster. *Phys. Chem. Chem. Phys.* **2010**, 12, 6219–6219.
- (39) Tofanelli, M. A.; Ni, T. W.; Phillips, B. D.; Ackerson, C. J. Crystal Structure of the $PdAu_{24}(SR)_{18}^{0}$ Superatom. *Inorg. Chem.* **2016**, 55, 999–1001.
- (40) Qian, H.; Jiang, D. E.; Li, G.; Gayathri, C.; Das, A.; Gil, R. R.; Jin, R. Monoplatinum Doping of Gold Nanoclusters and Catalytic Application. *J. Am. Chem. Soc.* **2012**, *134*, 16159–16162.
- (41) Christensen, S. L.; MacDonald, M. A.; Chatt, A.; Zhang, P.; Qian, H.; Jin, R. Dopant Location, Local Structure, and Electronic Properties of Au₂₄Pt(SR)₁₈ Nanoclusters. *J. Phys. Chem. C* **2012**, *116*, 26932–26937.
- (42) Yao, Q.; Feng, Y.; Fung, V.; Yu, Y.; Jiang, D.-e.; Yang, J.; Xie, J. Precise Control of Alloying Sites of Bimetallic Nanoclusters via Surface Motif Exchange Reaction. *Nat. Commun.* **2017**, *8*, 1555.

- (43) Yao, Q.; Yuan, X.; Fung, V.; Yu, Y.; Leong, D. T.; Jiang, D. E.; Xie, J. Understanding Seed-Mediated Growth of Gold Nanoclusters at Molecular Level. *Nat. Commun.* **2017**, *8*, 927.
- (44) Kim, M.; Tang, Q.; Narendra Kumar, A. V.; Kwak, K.; Choi, W.; Jiang, D.-e.; Lee, D. Dopant-Dependent Electronic Structures Observed for $M_2Au_{36}(SC_6H_{13})_{24}$ Clusters (M = Pt, Pd). *J. Phys. Chem. Lett.* **2018**, *9*, 982–989.